

Nickel-organic Frameworks with Hierarchical Flowers Structure Fabricated by Surfactant-assisted Solvothermal Method for High-performance Supercapacitors

Yi Wu¹, Xiangpeng Ding¹, Yumei Luo^{1,2}, Fen Xu^{1,2,*}, Lixian Sun^{1,2,*}, JianHao Lao¹, Xiaohui Qin¹, Cai Dan^{1,2,*}, Yu Wang¹, Qingqing Yin¹, Tao Wang¹, Kexiang Zhang^{1,2}, Bin Li^{1,2}, Huanzhi Zhang^{1,2}, Yongjin Zou^{1,2}

¹ School of Material Science and Engineering, Guilin University of Electronic Technology, Guilin, 541004, P. R. China.

² Guangxi Key Laboratory of Information Materials, Guangxi Collaborative Innovation Center of Structure and Property for New Energy and Materials.

*E-mail: xufen@guet.edu.cn or 1732211579@qq.com, sunlx@guet.edu.cn, Dancai1985@guet.edu.cn

Received: 17 November 2020 / Accepted: 12 January 2021 / Published: 31 January 2021

In this work, Ni-MOF (R-160) with a hierarchical flower-like structure is fabricated by a facile solvothermal method with surfactant assistance. Benefiting from its structure, R-160 has a very high specific surface area and a large number of exposed active sites. Electrochemical research results show that the electrochemical performance of R-160 prepared with sodium dodecyl sulfate (SDS) is superior to that of B-160 prepared without SDS assistance. For instance, the specific capacitance of B-160 is only 808 F g⁻¹ at a current density of 1 A g⁻¹. Nevertheless, the specific capacitance of R-160 reaches 1036 F g⁻¹ under the same conditions, which is 28.2% higher than that of B-160. Moreover, the energy density of an asymmetric device assembled with R-160 and AC is 38.3 W h kg⁻¹ at a power density of 749.9 W kg⁻¹.

Keywords: nickel-metal-organic framework; surfactant; solvothermal method; supercapacitor

1. INTRODUCTION

With the rapid development of global industrialization, the utilization rate of energy has sharply increased. However, the current global industry is still driven by fossil fuels such as coal, oil, and natural gas. As the reserves of nonrenewable energy sources such as fossil fuels are increasingly decrease, environmental pollution, catastrophic climate change and other problems are becoming increasingly serious; thus, humankind has to face these problems and attempt to use renewable energy sources that can replace fossil fuels. However, currently, most renewable clean energy cannot provide a stable and continuous supply, owing to time and geography limitations [1]. Therefore, it is necessary to develop a device that can utilize clean energy conversion and storage to make full use of these intermittent energy

sources [2]. For many energy storage devices, supercapacitors have been increasingly studied due to their advantages, such as their high power density, wide operating temperature, and high charge/discharge rates. Among the various electrode materials, those with high power density and energy density are key for producing high-performance supercapacitors.

Metal organic frameworks (MOFs) are porous materials connected by metal units and organic ligands and feature a large surface area, an adjustable aperture and an orderly crystal structure. MOFs are widely used in various applications, including gas storage [3], proton conduction [4], and sensors [5]. MOFs have become a focus in research because of their diverse topological structures and abundant metal ions; however, they are seldom used directly as electrode materials due to their poor electrical conductivity. In 2010, Kobayashi et al [6] synthesized an MOF with an optical band gap and doped I₂ into it. This material only preliminarily solved the conduction problem of MOFs. Since then, MOFs have been applied in the field of supercapacitors (SCs) as electrode materials. Numerous studies have reflected that the electrochemical properties of MOFs are largely influenced by metal sites and organic ligands.

Metals such as Mn [7], Fe [8], Co [8,9], Ni [10-12], Zn [13] and Cu [14] can provide active sites for redox reactions during electrochemical energy storage. Nickel, as a transition metal element and an important component of Ni-MOF, provides a good metal site due to the abundant valences of Ni (namely, Ni²⁺ or Ni³⁺). Yang and her partners [15] successfully synthesized a new nickel-based nanosheet MOF (Ni₃(OH)₂BDC₂) for use in high-performance supercapacitors and found that it provided a high specific capacitance of 1127 F g⁻¹ at a current density of 0.5 A g⁻¹ and maintained 90% capacitance after 3,000 cycles. They demonstrated that this MOF (Ni₃(OH)₂BDC₂) had a typical 2D nanosheet structure. In this structure, the electrons were confined to conducting within the nanosheets, leading to the material having excellent conductivity. Moreover, the unique layered structure of the above MOF was conducive to increasing the effective contact area with the electrolyte. Thus, more active sites participated in the electrochemical reaction, which provides the material with excellent electrochemical characteristics.

Auxiliaries play an important role in the morphology regulation of nanosheet materials. The “coordination equilibrium” seen in organic ligands and metal-ion units is affected by the action of ligand closure. The epitaxial growth orientation and the crystal growth rate of MOFs can be regulated by various assistant agents. In situ growth is the key factor controlling the size and morphology of inorganic and organic nanoparticles. The interactions between organic ligands and metal ions or ionic matrices in mixed solutions vary with the addition of surfactants.

Zheng's team [16] used polyethylene pyrrolidone (PVP) to regulate ultrathin 2D-Co-MOF. They found that adjusting the surfactant via a hydrothermal method could promote the vertical growth of MOFs, which could also effectively control the thickness of the nanosheet. Additionally, the open layer spacing could also accommodate an abundance of anions. The presence of anions can provide additional electrochemically active sites and enhance the hydrophilicity of the material, making the prepared electrode more easily wetted by an aqueous electrolyte.

In this work, we report that the Ni-MOF structure can be controlled by anionic surfactants. This control method is based on the coordination of Ni²⁺ and 1,3-phthalic acid (PTA) by a one-step hydrothermal method using anionic surfactants. The utilization of the static sealing effect between the negatively charged anionic surfactant head groups and metal ions inhibits the growth of crystals on a crystal surface, finally synthesizing Ni-MOF with a nanoscale lamellar flower-like structure.

Importantly, this method can still maintain the openness of the nanocluster structure even at high temperatures while preventing the stacking of nanosheets. Therefore, the obtained Ni-MOF has a large specific surface area and good electrochemical properties. When used as an electrode material in supercapacitors, the as-prepared Ni-MOF with a lamellar flower-like structure shows a high specific capacitance of 1036 F g^{-1} at a current density of 1 A g^{-1} and provides an energy density of 38.3 W h kg^{-1} at a power density of 749.9 W kg^{-1} . Hence, Ni-MOF with a nanoscale lamellar flower-like structure is a promising electrode material for use in supercapacitors.

2. EXPERIMENTAL

2.1 Materials

Nickel acetate tetrahydrate ($\text{Ni}(\text{C}_2\text{H}_3\text{O}_2)_2 \cdot 4\text{H}_2\text{O}$, analytical grade), 1,3-phthalic acid (PTA, analytical grade), sodium dodecyl sulfate (SDS), activated carbon (AC) and N,N-dimethylformamide (DMF) were purchased from Aladdin Company. Ethanol ($\text{CH}_3\text{CH}_2\text{OH}$, 99.8%) and potassium hydroxide (KOH, analytical grade) were obtained from Xilong Science Co., Ltd. All purchased reagents were not purified by additional treatment. All aqueous solutions were prepared by using ultrapure water (DI water, resistance of $18 \text{ M}\Omega \text{ cm}^{-1}$).

2.2. Typical synthesis of Ni-MOF

Ni-MOF was synthesized by a simple solvothermal method (as shown in Fig. 1). In a typical procedure, 0.0830 g (0.75 mmol) of PTA was dissolved in 30 ml of DMF/ethanol (1:1, v/v) with stirring at room temperature; this mixture was called the PTA solution. $\text{Ni}(\text{C}_2\text{H}_3\text{O}_2)_2 \cdot 4\text{H}_2\text{O}$ (0.1326 g, 0.5 mmol) was dissolved in 15 mL of water to obtain a nickel acetate solution. Then, the nickel acetate solution was slowly added into the above PTA solution with stirring. The mixture (approximately 80 mL) was next transferred to a Teflon-lined steel autoclave and kept for 24 h at different temperatures. After cooling naturally to room temperature, the resulting precipitate was sequentially washed several times with DMF, water and alcohol. Finally, the precipitate was dried in a vacuum drying chamber at $60 \text{ }^\circ\text{C}$ for 12 h to obtain a pale-green powdery sample (Ni-MOF). The Ni-MOF sample, which was synthesized at $160 \text{ }^\circ\text{C}$, was named B-160.

2.3. SDS-assisted synthesis of Ni-MOF

The experimental process of the SDS-assisted synthesis of Ni-MOF was similar to the above Ni-MOF synthesis. The difference was that 0.25 g of SDS surfactant was added to the mixed nickel acetate and PTA solution. The Ni-MOF obtained by SDS assistance was named R-160.

2.4. Material characterization

Powder X-ray diffraction (XRD, D8 Advance Bruker) was conducted to provide a microstructural analysis of the samples; XRD was conducted at 40 kV and 40 mA with a $\text{Cu K}\alpha$ radiation

source ($\lambda = 0.15406$ nm). The 2θ range was $5-90^\circ$ at a step size of 0.02° . Fourier transform infrared (FT-IR) spectroscopy of the samples was performed on a Thermo Fisher Nicolet 6700 spectrometer with KBr pellets. Thermogravimetric (TG) measurements were carried out in a temperature range of $25-900^\circ\text{C}$ in an atmosphere of N_2 at a $5^\circ\text{C}/\text{min}$ heating rate. The morphologies of B-160 and R-160 were characterized by scanning electron microscopy (SEM, SU8010, HITACHI) and transmission electron microscopy (TEM, Tecnai G2 F20, FEI Company), and their elemental analysis was also carried out by energy-dispersive X-ray spectroscopy (EDS). Nitrogen adsorption-desorption isotherms were measured with a gas adsorption analyzer (Autosorb iQ2, Quantachrome sorptometer) at 77 K. Before the measurement, the samples were degassed at 80°C for 2 h. The specific surface area (SSA) and pore size were calculated by the Brunauer-Emmett-Teller (BET) and Barrett-Joyner-Halenda (BJH) equations based on the adsorption branches of the isotherms. The qualitative analysis of elements was performed by X-ray photoelectron spectroscopy (XPS, ESCA 250, Scienta Omicron GmbH).

2.5 Electrochemical measurements

The electrochemical performance was investigated with a CHI 660E instrument utilizing a three-electrode system, and galvanostatic charge-discharge (GCD), cyclic voltammogram (CV) and electrochemical impedance (EIS) measurements were obtained. A platinum electrode was chosen as the counter electrode, and a Hg/HgO electrode was used as the reference electrode. A 3 M KOH aqueous solution was used as the electrolyte. The working electrode was prepared by mixing active material, acetylene black and polytetrafluoroethylene (PTFE) at a weight ratio of $80:10:10$ and then coating the slurry on ($1\text{ cm}\times 1\text{ cm}$) nickel foam to form a thin foil at a pressure of approximately 10.0 MPa.

The specific capacity of the electrode material was calculated by using the GCD results with Eqs. (1) and (2):

$$C_a = \frac{I \times \Delta t}{S \times \Delta V} \quad (1)$$

$$C_s = \frac{I \times \Delta t}{m \times \Delta V} \quad (2)$$

where C_a ($\text{F}\cdot\text{cm}^{-1}$), C_s ($\text{F}\cdot\text{g}^{-1}$), I (A) and S (cm^{-2}) represent the area specific capacity, mass specific capacity, discharge current and contact surface area of the working electrode, respectively. In addition, m (g^{-1}) is the mass of active material and Δt (s) and ΔV (V) are the discharge time and voltage range, respectively.

An asymmetric supercapacitor device was assembled by using the prepared Ni-MOF as a positive electrode and activated carbon as a negative electrode. The mass ratio of the positive electrode and negative electrode was required to meet Eq. (3) based on the charge balance $q^+ = q^-$:

$$\frac{m^+}{m^-} = \frac{\Delta V^- \times C^-}{\Delta V^+ \times C^+} \quad (3)$$

where m^+ , m^- , ΔV^+ , ΔV^- , C^+ and C^- are the masses, potentials, and specific capacitances for the positive electrode and negative electrode, respectively.

The energy density (E) and power density (P) are determined by Eqs. (4) and (5):

$$E = \frac{C_s \times \Delta V^2}{2 \times 3.6} \quad (4)$$

$$P = \frac{3600E}{\Delta t} \quad (5)$$

where C_s is the total capacitance of the asymmetric supercapacitor, ΔV is the potential window and Δt is the discharge time.

3. RESULTS AND DISCUSSION

3.1. Structure and morphology

Fig. 1a shows the XRD patterns of Ni-MOF [12], B-160 and R-160. Comparing B-160 and R-160 with the Ni-MOF reported in [12], B-160 and R-160 are consistent with $[\text{Ni}_3(\text{OH})_2(\text{C}_8\text{H}_4\text{O}_4)_2(\text{H}_2\text{O})_4]$ (CCDC No. 638866) [12]. This result shows that the structures of B-160 and R-160 are the same as those in the literature [12]. The FT-IR spectra of B-160 and R-160 are presented in Fig. 1b. The peaks at 3608 and 1500 cm^{-1} are ascribed to the stretching vibrations of the O-H and para-benzene C-H groups, respectively; the absorption peaks near 3435 and 3070 cm^{-1} indicate the presence of coordinated H_2O within the prepared Ni-MOFs. The strong bands at 1582 and 1390 cm^{-1} belong to the *vas* (-COO-) and *vs* (-COO-) groups, respectively. This result indicates that the -COO- of para-BDC is in a bidentate coordination mode. There are no obvious absorption peaks near 1257-1210 cm^{-1} (due to the vibration of S=O) in the FT-IR spectra for the prepared Ni-MOFs, indicating that there is no residual dodecyl sulfate group from SDS in B-160 and R-160. Taking R-160 as an example for XPS analysis, Fig. 1c shows that R-160 has three distinct peaks: a Ni 2p peak at 856 eV, an O 1s peak at 533 eV and a C 1s peak at 285 eV. The above results imply that Ni is successfully coordinated with PTA.

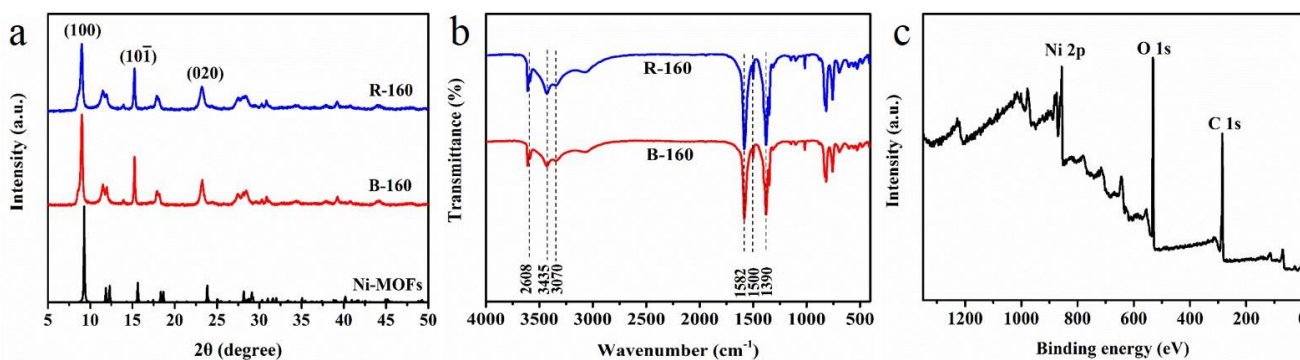


Figure 1. a: XRD patterns of Ni-MOF [12], B-160 and R-160; b: FT-IR spectra of B-160 and R-160; and c: XPS survey spectrum of R-160.

To confirm the amount of crystal water and NiO in R-160, TG analysis of R-160 was performed, as shown in Fig. 2. According to Fig. 2, the weight loss of the prepared Ni-MOF during the first two steps corresponds to the temperature ranges of 375-430 K and 430-545 K (Eqs. (6) and (7)), respectively). The corresponding dehydration amounts are 5.6% and 6.0%, respectively, which are consistent with the theoretical value for both (5.9%). The structure of the prepared Ni-MOF begins to collapse until approximately 700 K (see Eq. (8)). The residual is NiO, corresponding to a value of 37.1%, and this result is also in good agreement with the theoretical value (36.7%). This result further demonstrates that Ni-MOF is synthesized successfully and is the same as the Ni-MOF in [12].

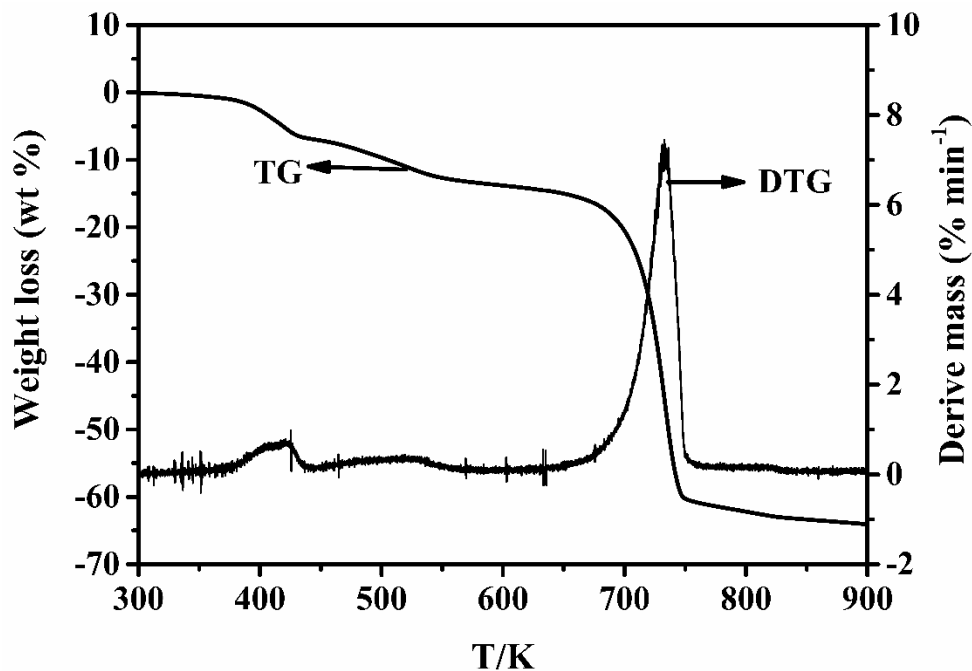


Figure 2. TGA curve of R-160.

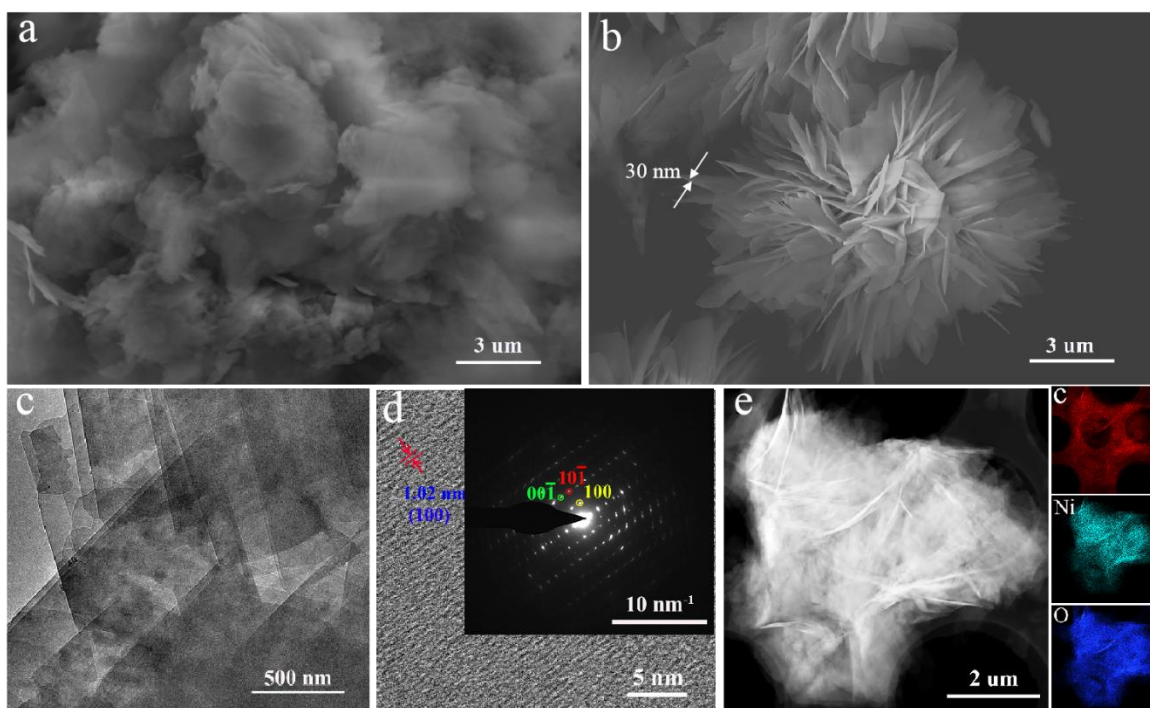
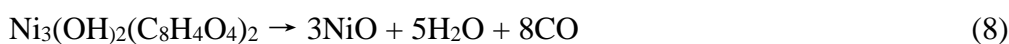
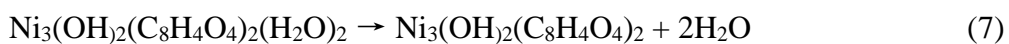
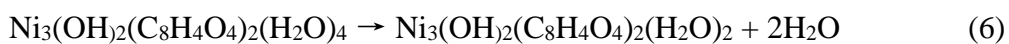


Figure 3. Morphology of the samples: a: SEM images of B-160; b: SEM images of R-160; c: TEM of R-160; d: HRTEM and SAED of R-160; and e: EDS mapping of the C, Ni and O in R-160.

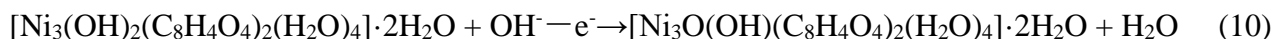
The SEM images of B-160 and R-160 are shown in Fig. 3a and 3b. It can be found that R-160 exhibits a hierarchical flower-like structure assembled by nanosheets with a uniform thickness of approximately 30 nm and an abundance of gaps; however, B-160 without SDS assistance is stacked randomly and has barely visible gaps. This observation demonstrates that SDS has a significant impact on the structural modification of Ni-MOF. The flower-like structure of R-160 with SDS assistance can prevent the formation of parallel plate-like structures and the agglomeration of nanosheets. Moreover, the structure can still shorten the path of ion diffusion and expose an abundance of metal sites, which is favorable for surface-controlled Faradaic capacitance [17,18]. In addition, the layered nanoflowers have more open structures and larger plate spacing than B-160, which also provides a good environment for the diffusion of ions in energy storage reactions. A main reason for producing this flower-like structure is that the hydrophilic negative group SO_4^{2-} is adsorbed on the positive metal ion Ni^{2+} at the end of the compound by electrostatic adsorption, and the hydrophobic dodecyl group is oriented toward the solution [19]. The end-capping reaction promotes anisotropic crystal growth and the formation of nanosheets, thereby providing the formation of a hydrophobic micelle structure on the MOF surface. However, according to FT-IR analysis, there is no hydrophobic dodecyl group on the surface of R-160, and we speculate that the group may be washed off during the R-160 purification process. Therefore, the dodecyl group will induce partial crystal exposure of R-160, and it is predicted that this kind of structure will be favorable for the transport of electrons and the diffusion of electrolyte solutions.

The TEM images of R-160 also illustrate that R-160 is composed of many nanosheets (see Fig. 3c). Its HRTEM image and selected area electron diffraction (SAED) pattern show diffraction spots attributed to the (100), $(00\bar{1})$ and $(10\bar{1})$ planes (see Fig. 3d). The lattice spacing of the (100) plane in the XRD patterns is 1.02 nm, which is consistent with the lattice spacing of the Ni-MOF in [12]. The EDS images of R-160 are shown in Fig. 3e, proving that Ni, C and O are evenly distributed in R-160.

The specific surface area and pore structure are two principal elements that affect capacitance; a nitrogen adsorption-desorption experiment was applied to determine the BET surface area and pore features of R-160 and B-160. Based on the typical N_2 adsorption-desorption curves of B-160 and R-160, the BET surface area of R-160 is $40.1 \text{ m}^2 \text{ g}^{-1}$, which is larger than that of B-160 ($36.4 \text{ m}^2 \text{ g}^{-1}$). This result illustrates that the hierarchical flower-like structure of R-160 increases the specific surface area of Ni-MOF. The pore diameter of R-160 (3.8 nm) is also greater than that of B-160 (2.5 nm). Mesopores are beneficial for ion diffusion; thus, the electrochemical performance of R-160 will be superior to that of B-160.

3.2 Electrochemical measurements

The electrochemical performance of R-160 and B-160 was studied in a three-electrode cell with a 3.0 M KOH solution as the electrolyte (Fig. 4). From Fig. 4a, the CV curves of R-160 and B-160 all appear as an obvious pair of redox peaks, indicating that both materials have a reversible charge-discharge reaction and demonstrate pseudocapacitive-type capacitance. In addition, the reaction is as follows:



The redox peak area of R-160 is much larger than that of B-160, which also demonstrates that R-160 possesses better electrochemical performance because of the structural differences [20]. The GCD curves of R-160 and B-160 are summarized in Fig. 4b at a current density of 1 A g^{-1} . Based on Fig. 4b, the specific capacity of R-160 is calculated to be 1036 F g^{-1} , which is 28.2% higher than that of B-160 (808 F g^{-1}). At the same time, it can be found that R-160 still maintains a good specific capacity (680 F g^{-1}) even at a high current of 10 A g^{-1} (Fig. 4c), and the capacitance retention is 66% of the specific capacity at 1 A g^{-1} (Fig. 4c and 4d). The decrease in capacitance with increasing current density is mainly due to the low utilization rate of the active material during fast charge and discharge [21].

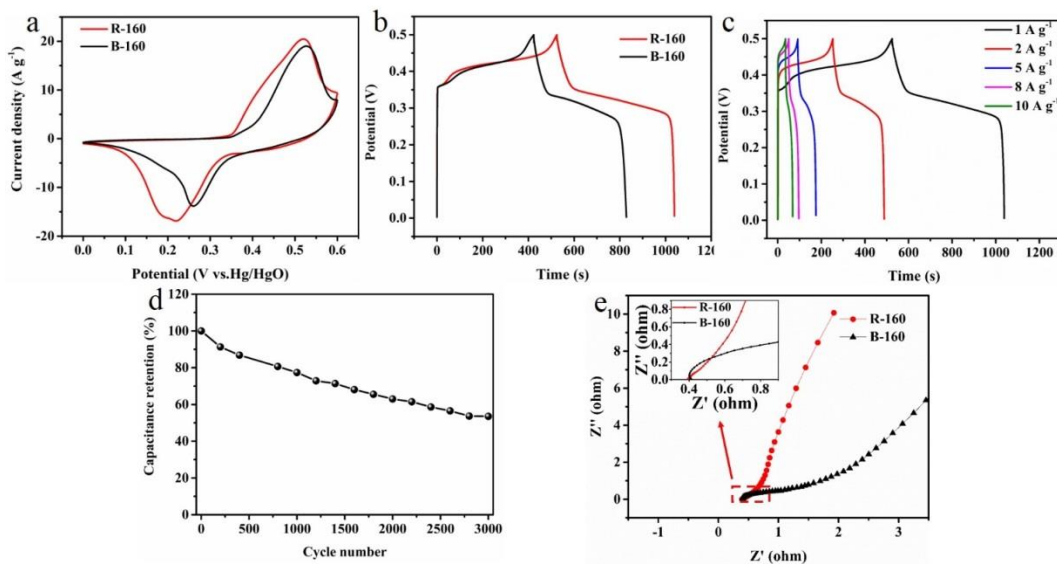


Figure 4. Electrochemical performance of R-160 and B-160: a: CV curves at 5 mV s^{-1} ; b: GCD curves at 1 A g^{-1} ; c: GCD curves of R-160; d: cycling stability of R-160; and e: EIS curves.

From Fig. 4c, the current density of R-160 at the redox peak increases with an increasing scan rate, indicating that the electrode material has low resistance. The EIS spectrum (Fig. 4e) consists of a semicircle in the high-frequency region corresponding to the charge-transfer resistance and a straight line in the low-frequency region reflecting the diffusion resistance at the electrode/electrolyte interface [22]. Comparing the EIS curve of R-160 to that of B-160, the R_{ct} values of R-160 and B-160 are 1.04Ω and 1.76Ω , respectively. This result shows that R-160 has a lower charge-transfer resistance than B-160. Additionally, the straight line of R-160 in the low-frequency region is closer to 90° than that of B-160, which shows that the diffusion resistance of R-160 is lower than that of B-160; that is, Ni-MOF with SDS assistance is more conducive to the diffusion of electrolyte ions. This observation is because R-160 has a more open structure (Fig. 3b), and this open structure leads to faster ion diffusion and lower transfer/diffusion resistance [23]. The above results demonstrate that R-160 has better energy storage performance than B-160.

To study the practical capability of R-160, an asymmetric supercapacitor is assembled by employing the as-synthesized R-160/nickel foam (NF) as the positive electrode and activated carbon (AC)/NF as the negative electrode; the electrolyte is a 3.0 M KOH aqueous solution. The CV curves of the asymmetric supercapacitor in different potential windows at sweep rates of 5 mV s^{-1} are shown in Fig. 5a. Fig. 5a shows the hybrid energy storage behavior of the asymmetric supercapacitor, which

includes pseudocapacitance and electric double-layer capacitance characteristics, as reported in the literature [24]. Furthermore, the results also show that the supercapacitor can stably extend to a large voltage window of 1.7 V. From the GCD curves (Fig. 5b), the specific capacitances are calculated to be 122.6, 106.6, 87.46 and 66.1 F g⁻¹ and correspond to current densities of 1, 2, 5 and 8 A g⁻¹, respectively; these results are also shown in Fig. 5c. Fig. 5c demonstrates that the asymmetric supercapacitor can power a light-emitting diode (LED).

Cycling life is a significant feature of supercapacitors. From Fig. 5d, it can be found that the asymmetric supercapacitor has better cycling stability with a retention of 50% at a current density of 3 A g⁻¹ after 3000 cycles and a high coulombic efficiency of 99%. Fig. 5e reveals that the impedance R_{ct} of the device is 7.52 Ω, which is beneficial to electron transfer. The energy density of the supercapacitor is 38.3 W h kg⁻¹ at a power density of 749.9 W kg⁻¹. Compared to the Ni-MOF and Co-Ni-MOF in [25, 26, 27, 28, 29, 30] (Fig. 5f), the R-160 prepared in this work possesses very good energy storage. Consequently, a new preparation method of Ni-MOF as an electrode material for supercapacitors is presented in this work.

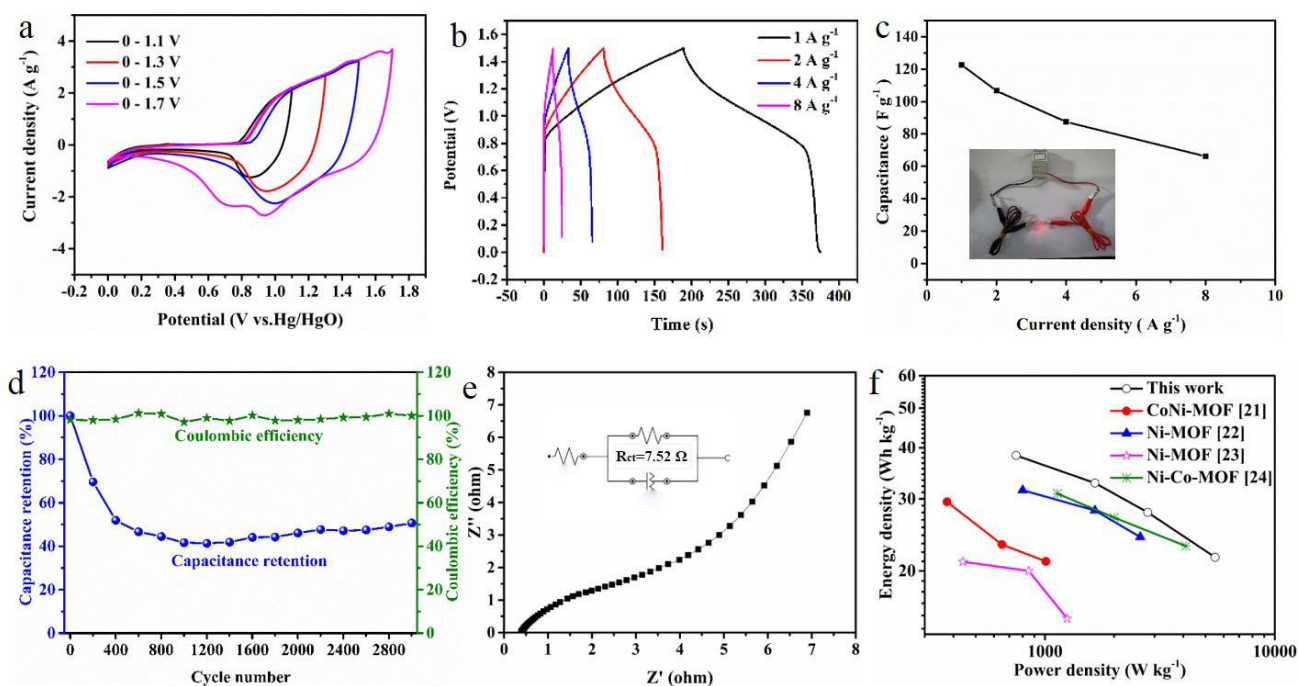


Figure 5. Electrochemical performances of the asymmetric supercapacitor: a: CV curves in different potential windows at 5 mV s⁻¹; b: GCD curves; c: specific capacitance at various current densities; d: cycling stability at a current density of 3 A g⁻¹; e: EIS curves; and f: Ragone plots of the material in this work and in the literature.

4. CONCLUSIONS

In summary, nanosheet-stacked flower-like Ni-MOF was successfully fabricated by a solvothermal method with surfactant (SDS) assistance in this work. The structural and morphological analysis demonstrated the effectiveness of SDS doping during the hydrothermal synthesis of Ni-MOF.

The electrochemical performance of Ni-MOF as a supercapacitor electrode material was tested. The results illustrated that the electrochemical performance of Ni-MOF (R-160) prepared with SDS assistance was superior to that of Ni-MOF (B-160) prepared without SDS assistance. For example, the specific capacitance of B-160 was only 808 F g⁻¹ at a current density of 1 A g⁻¹. However, the specific capacitance of R-160 reached 1030 F g⁻¹ under the same conditions, and its capacity retention was 50% (up to 3000 cycles at 3 A g⁻¹). An asymmetric supercapacitor assembled by R-160 and AC achieved an energy density of 38.3 W h kg⁻¹ at a power density of 749.9 W kg⁻¹. It is foreseen that the current approach will provide valuable insights into the structural and nanomorphological control of MOFs for energy storage technologies and beyond.

ACKNOWLEDGEMENTS

This work was financially supported by the National Key Research and Development Program of China (2018YFB1502103, 2018YFB1502105), the National Natural Science Foundation of China (51671062, 51871065 and 51971068), the Scientific Research and Technology Development Program of Guangxi (AA19182014, AD17195073, AA17202030-1), Guangxi Bagui Scholar Foundation, Guangxi Collaborative Innovation Centre of Structure and Property for New Energy and Materials, Guangxi Advanced Functional Materials Foundation and Application Talents Small Highlands, Chinesisch-Deutsche Kooperationsgruppe (GZ1528) and Innovation Project of GUET Graduate Education (2020YCXS112).

References

- 1 G. Andreas, H. Llewelyn, *Nature*, 588 (2020) 28.
- 2 H. Wan, F. S. Chen, W. Ma, X. H. Liu, R. Z. Ma, *Nanoscale*, 12(2020)21479.
- 3 J. Yang, Y. W. Yang, *Small*, 16 (2020) 1906846.
- 4 J. A. Hurd, R. Vaidhyananathan, V. Thangadurai, C. I. Ratcliffe, I. L. Moudrakovski, G. K. H. Shimizu, *Nat. Chem.*, 1 (2009) 705.
- 5 L. E. Kreno, K. Leong, O. K. Farha, M. Allendorf, R. P. V. Duyne, J. T. Hupp, *Chem. Rev.*, 112 (2012) 1105.
- 6 Y. Kobayashi, B. Jacobs, M. D. Allendorf, J. R. Long, *Chem. Mat.*, 22 (2010) 4120.
- 7 S. Shashank, M. Sunita, D. Akash, *Energy Procedia*, 158 (2019) 5817.
- 8 D. Y. Lee, S. J. Yoon, N. K. Shrestha, S. H. Lee, H. Ahn, S. H. Han, *Microporous Mesoporous Mat.*, 153 (2012) 163.
- 9 D. Lee, D. V. Shinde, E. Kim, W. Lee, I. Oh, N. K. Shrestha, *Microporous Mesoporous Mat.*, 171 (2013) 53.
- 10 C. M. Liao, Y. K. Zou, W. Zhang, J. C. Zhao, B. Tang, A. Tang, Y. H. Song, J. L. Xu, *Russ J Electrochem.*, 49 (2013) 983.
- 11 J. Xu, C. Yang, Y. F. Xue, C. Wang, J. Y. Cao, Z. D. Chen, *Electrochim. Acta*, 211 (2016) 595.
- 12 J. Yang, P. Xiong, C. Zheng, H. Y. Qiu, M. D. Wei, *J. Mater. Chem. A.*, 2 (2014) 16640.
- 13 Y. Gong, J. Li, P. G. Jiang, Q. F. Li, J. H. Lin, *Dalton Trans.*, 42 (2013) 1603.
- 14 D. Y. Fu, H. W. Li, X. M. Zhang, G. Y. Han, H. H. Zhou, Y. Z. Chang, *Mater. Chem. Phys.*, 179 (2016) 166.
- 15 J. Yang, P. Xiong, C. Zheng, H. Y. Qiu, M. D. Wei, *J. Mater. Chem. A.*, 2 (2014) 16640.
- 16 Y. Zheng, S. S. Zheng, Y. X. Xu, H. G. Xue, C. S. Liu, H. Pang, *Chem. Eng. J.*, 373 (2019) 1319.
- 17 H. T. Niu, Y. Zhang, Y. Liu, B. F. Luo, N. Xin, W. D. Shi, *J. Mater. Chem. A.*, 7 (2019) 8503.
- 18 Z. H. Pan, J. Yang, Q. C. Zhang, M. N. Liu, Y. T. Hu, Z. K. Kou, N. Liu, X. Yang, X. Y. Ding, H. Chen, *Adv. Energy Mater.*, 9 (2019) 9.

- 19 N E Shi, W Du, X L Jin, Y Zhang, M Han, Z Xu, L H Xie, Huang W, *Cryst. Growth Des.*, 14 (2014) 1251.
- 20 L. Ben, C. L. Wu, M. Li, L. F. Jia, G. P. Wang, *Int. J. Electrochem. Sci.*, 15 (2020) 5758.
- 21 Q. Y. Wang, Y. M. Luo, R. Z. Hou, S. Zaman, K. Qi, H. F. Liu, H. S. Park, B. Y. Xia, *Adv. Mater.*, 31 (2019) 1905744.
- 22 L. S. Xie, L. Sun, R. M. Wan, S. S. Park, J. A. Degayner, C. H. Hendon, M. Dinca, *J. Am. Chem. Soc.*, 140 (2018) 7411.
- 23 Y. N. Shen, X. L. Miao, D. D. Song, Y. T. Li, Y. N. Qu, J. G. Yu, J. J. Tang, H. Qin, L. L. Wang, J. H. Ren, B. Wang, *Int. J. Electrochem. Sci.*, 14 (2019) 2767.
- 24 L. H. Lin, X. L. Yao, L. Ma, *Int. J. Electrochem. Sci.*, 15 (2020) 7763.
- 25 C. T. Ren, X. Jia, W. Zhang, D. Hou, Z. Q. Xia, D. S. Huang, J. Hu, S. P. Chen, S. L. Gao, *Adv. Funct. Mater.*, 30 (2020) 2004410.
- 26 J. Wang, Q. Zhong, Y. H. Xiong, D. Y. Cheng, Y. Q. Zeng, Y. F. Bu, *Appl. Surf. Sci.*, 483 (2019) 1158.
- 27 S. W. Gao, Y. Z. Sui, F. X. Wei, J. Q. Qi, Q. Q. Meng, Y. Z. Meng, *J. Mater. Sci.*, 53 (2018) 6807.
- 28 P. C. Du, Y. M. Dong, C. Liu, W. L. Wei, D. Liu, P. Liu, *J. Colloid Interface Sci.*, 518 (2018) 57.
- 29 C. Chen, L. Han, K. Tao, J. J. Zhou, Y. L. Li, X. Han, L. Han, *Dalton Trans.*, 47 (2018) 5639.
- 30 Q. Chong, J. Yang, B. Zhao, D. C. Chen, R. Q. Zou, K. S. Walton, M. Liu, *Nano Energy*, 26 (2016) 66.
- 31 Y. Yan, P. Gu, S. S. Zheng, M. B. Zheng, H. Pang, H. G. Xue, *J. Mater. Chem. A.*, 4 (2016) 19078.

© 2021 The Authors. Published by ESG (www.electrochemsci.org). This article is an open access article distributed under the terms and conditions of the Creative Commons Attribution license (<http://creativecommons.org/licenses/by/4.0/>).